Desalination and Water Treatment
www.deswater.com

doi: 10.1080/19443994.2013.822170

51 (2013) 6444–6458
October

Taylor & Francis
Taylor & Francis Group

Comparison of nonhomogeneous and homogeneous mass transfer in reverse osmosis membrane processes

Yuming Fang, Steven J. Duranceau*

Department of Civil, Environmental and Construction Engineering, University of Central Florida, PO Box 162450, Orlando, FL 32816-2450, USA
Tel. +1 407 823 1440; Fax: +1 407 823 3315; email: steven.duranceau@ucf.edu

Received 24 April 2013; Accepted 4 June 2013

ABSTRACT

Reverse osmosis (RO) membranes are pressure driven, diffusion controlled processes. Current diffusion controlled solute mass transfer models assume a homogeneous membrane surface. This study evaluated mass transfer processes assuming mass transport is not a homogeneous process, which is dependent on the thickness variation of the membrane's active layer. Three-dimensional ridge and valley active layer morphologies were created numerically using Gaussian random vectors. A nonhomogeneous solution diffusion model (NHDM) was then developed to account for surface variation through the active layer. NHDM was further modified by incorporating concentration polarization (CP) effects. A comparison of the NHDM and the NHDMCP with the commonly accepted homogeneous solution diffusion model (HSDM) using pilot-scale brackish water RO operating data indicated that the NHDM is more accurate, when the solute concentration in the feed stream is low, while NHDMCP appears to predict better with a high solute feed concentration.

Keywords: Membrane active-layer; Reverse osmosis; Mass transfer coefficients; Nonhomogeneous; Gaussian random vector; Concentration polarization

1. Introduction

The relationship between solvent and solute mass transfer with the physical and chemical conditions of reverse osmosis (RO) membranes are complicated and not completely understood. In RO membrane processes, solute permeation, or salt passage, is controlled by diffusion as a result of the concentration gradient across the membrane surface [1–6]. Mathematical models have been developed to predict permeate solute concentration assuming a constant mass transfer coefficient (MTC) based on a flat membrane surface. The governing theory is based upon a mass transport differential equation expressed in terms of mass change per unit time and includes advection and diffusion terms; these models are solved using either a dynamic or steady-state assumption. Models that include the dynamic assumption describe the solute concentration as a function of operating time and space, and the mass transport equation is solved numerically [3,7,8]. The steady state assumption represents a simpler approach and assumes laminar flow conditions, whereby allowing the mass transport equation to be solved analytically [2,4,9]. Other approaches integrate dimensional analysis into the

*Corresponding author.

mass transport equation to take into account different hydraulic flow conditions [10–13].

The majority of RO membranes are manufactured in a spiral-wound configuration using thin-film composite (TFC) technologies. A typical TFC membrane consists of three layers: the top polyamide layer is the active layer participating in the rejection of dissolved solutes, under the top layer is the polysulfone backing layer, and the polyester support layer [14–15]. Membrane material, surface characteristics, and source water properties can affect membrane permeability, rejection, and fouling behavior. There have been many studies in which the relationship between the surface structure and membrane permeability has been examined. Ghiu explored solute permeability in RO membranes and identified that membrane performance was impacted by surface properties [16]. The Atomic Force Microscopy (AFM) images presented in the study of Vrijerhoek et al. depict membrane surfaces as having an elevated ridge and depressed valley morphology. They concluded the fouling behavior was related to the degree of surface roughness [17]. Elimelech compared surface morphology of cellulose acetate RO membranes and composite polyamide RO membranes by AFM and scanning electron microscope (SEM) images and concluded the higher fouling rate for the TFC membranes is attributed to the degree of surface roughness [18]. These studies suggested that membrane permeability was indeed affected by the surface morphology, however, a method to numerically represent the membrane surface structure and its impact on solute MTCs has yet to be developed.

The objective of this study has three aspects: (1) to develop the nonhomogeneous solution diffusion model (NHDM) which incorporates surface roughness, (2) to modify the NHDM by incorporating the concentration polarization effect (NHDMCP) to take into account particle interaction in the diffusive layer where concentration polarization (CP) would be anticipated to exist, and (3) to compare with the homogeneous solution diffusion model (HSDM). To reach these goals, topographic surface morphologies of commercial RO membranes were incorporated into a diffusion-based model developed to account for variations in the membrane active-layer thickness. A higher degree of salt passage is experienced in the depressed valley portions of the membrane, where the active layer is the thinnest and activation energies are the lowest. The numerical investigations performed in this study along with model development were accomplished with MATLAB Ver. 7.10.0 (2010) [19]. Both NHDM and NHDMCP are modified versions of the HSDM, where the basic HSDM assumes a uniform membrane surface and constant MTCs. A detailed description of NHDM, NHDMCP, and HSDM are elucidated in the following sections.

2. Model development

Many different theories and models attempt to describe mass transfer in diffusion-controlled membrane processes. However, a few basic principles or theories are used to develop most of these models: convection, diffusion, film theory, and electroneutrality [20]. These principles or theories could be used to group models into linear diffusion models, exponential diffusion models, and coupling models. Most of the modeling efforts have been developed using lab or bench-scale testing equipment, and may or may not have incorporated product recovery, limiting their practical use. Fig. 1 depicts a general representation of mass transport flow through a membrane element, and will serve as the basis for mathematical representations used in this study.

2.1. Overview of the HSDM

Eqs. (1)–(5) are the governing equations used to derive the pressure driven, diffusion controlled, linear homogeneous solution diffusion model (HSDM) for a high recovery RO system [21–24]. These equations require a mass balance across the entire RO system. The solute MTC (K_s) represents the overall permeability of dissolved substances and can be experimentally determined. The HSDM was derived by Eqs. (7) and (8) is shown in Eq. (9). This model can be utilized to predict the solute permeate concentration (C_p), given feed concentration (C_f), net pressure ($\Delta p - \Delta\pi$), recovery (r), and MTCs (k_w, k_s).

$$F_w = k_w(\Delta p - \Delta\pi) = \frac{Q_p}{A} \tag{1}$$

$$J_s = k_s \Delta c = \frac{Q_p C_p}{A} \tag{2}$$

$$\Delta c = \frac{C_f + C_c}{2} \tag{3}$$

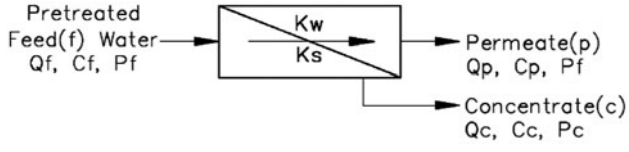

Fig. 1. Basic diagram of mass transport in a membrane.

$$r = \frac{Q_p}{Q_f} \tag{4}$$

$$Q_f = Q_c + Q_p \tag{5}$$

$$Q_f C_f = Q_c C_c + Q_p C_p \tag{6}$$

Combining Eqs. (1)–(3), C_p can be determined by Eq. (7):

$$C_p = \frac{k_s\left(\frac{C_f + C_c}{2}\right)}{F_w + k_s} \tag{7}$$

The retained solute concentration C_c can be determined by combing Eqs. (4)–(6), resulting in Eq. (8):

$$C_c = \frac{C_f - rC_p}{1 - r} \tag{8}$$

Substituting Eq. (8) into Eq. (7) and rearranging, the permeate concentration C_p can be determined by Eq. (9), which is the HSDM.

$$C_p = \frac{k_s C_f}{F_w\left(\frac{2-2r}{2-r}\right) + k_s} \tag{9}$$

2.2. NHDM development

The HSDM can be modified by incorporating the effect of a nonuniform membrane surface on the solute's permeability to produce NHDM. The entire membrane channel can be divided into small uniform slices using a finite difference method. Development of this model applies Eqs. (1)–(6) on a small uniform membrane slice of the membrane module to solve the water qualities at each slice. The divided membrane channel is depicted in Fig. 2, assuming homogeneous diffusion at each slice. In this representation, Q_i and Q_{i+1} represent the flow rate at the feed and retained side of the uniform slice, C_i and C_{i+1} are the solute concentration at the feed and retained side of the uniform slice in the bulk stream, A_i is the membrane effective area of uniform slice for salt rejection, where i denotes the computational iteration along the membrane channel.

The computational boundary is taken from one uniform slice of the membrane channel. Eqs. (1)–(6) therefore expressed as follows:

$$F_{wi} = k_{wi}(\Delta p_i - \Delta \pi_i) = \frac{Q_{pi}}{A_i} \tag{10}$$

$$J_i = k_{si}(C_i - C_{pi}) \tag{11}$$

$$r_i = \frac{Q_{pi}}{Q_i} \tag{12}$$

$$Q_{i+1} = Q_i - Q_{pi} \tag{13}$$

$$C_{i+1} = \frac{Q_i C_i - Q_{pi} C_{pi}}{Q_{i+1}} \tag{14}$$

The permeate concentration at each uniform slice is expressed as:

$$C_{pi} = \frac{k_{si} C_i}{F_{wi}\left(\frac{2-2r_i}{2-2r_i}\right) + k_{si}} \tag{15}$$

Osmotic pressure is defined in Eq. (16):

$$\Delta \pi_i = k_t(C_{ti} - C_{tpi}) \tag{16}$$

where k_t equals 0.01 $\frac{psi}{\frac{mg}{L}\text{TDS}}$ [25] and C_{ti} and C_{tpi} are the total dissolved solid (TDS) concentrations in the bulk and permeate stream. Approximating the net driven pressure $(\Delta p_i - \Delta \pi_i)$ by assuming $k_t C_{ti} \approx k_t(C_{ti} - C_{tpi})$ the permeate flow rate can be estimated with Eq. (17):

$$Q_{pi} = \frac{k_{wi}(\Delta p_i - k_t C_{ti})}{A_j} \tag{17}$$

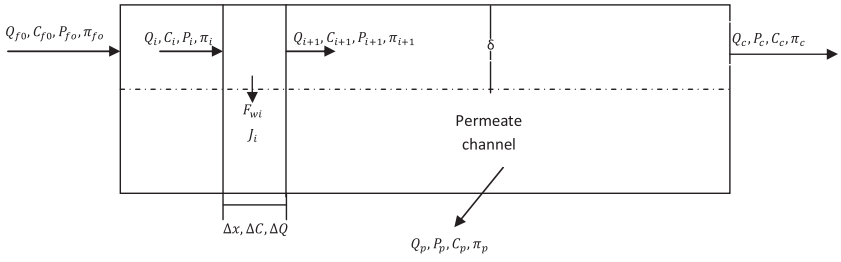

Fig. 2. Schematic representation of computational boundary of membrane channel.

The bulk flow (Q_i) can be correlated to the pressure drop along the membrane channel. As feed flow travels in the membrane channel, transmembrane pressure decreases due to the hydraulic friction loss. The transmembrane pressure profile in the membrane channel can be described by Eq. (18) [26]:

$$\Delta P_i = (P_f - P_p) - \frac{12k\mu v_i L}{nH^2} \tag{18}$$

where P_f and P_p are the feed and permeate pressure, k is the friction coefficient, μ is the fluid viscosity, L is the membrane channel length, H is the membrane channel height, and n is the number of uniform slices for channel discretization. With a known pressure at the end of the membrane channel and assuming the permeate pressure stays constant, the friction coefficient can be determined in Eq. (19):

$$k = \frac{(P_f - P_c)H^2}{12\mu v_c L} \tag{19}$$

where P_c is the retained pressure at the end of the membrane channel and v_c is the cross flow velocity at the end of the membrane channel. The cross flow velocity (v_i) can be calculated from the bulk flow rate (Q_i) in the membrane channel over the cross flow area and is expressed in Eq. (20):

$$v_i = \frac{Q_i}{WH} \tag{20}$$

where W is the membrane element width. Once Q_i and Q_{pi} have been solved, C_{pi} can be calculated by Eq. (15) with the following initial conditions:

$$C_0 = C_f;\ Q_0 = Q_f;\ \Delta P_0 = P_f - P_p \tag{21}$$

2.3. Development of NHDMCP

NHDM can be further modified by taking into account the CP effect. In the RO membrane process, CP leads to an increase in the osmotic pressure and thereby reduces the permeate flux. The expression of CP at the steady state is given by Eq. (22) [27]:

$$\frac{C_{mi} - C_{pi}}{C_i - C_{pi}} = \exp^{\frac{F_w \delta}{D}} = \exp^{\frac{F_w}{k_d}} \tag{22}$$

where C_{mi} is the concentration at the membrane surface, δ is the thickness of CP layer, D is the diffusivity of salt, and k_d is the MTC within the CP layer. The concentration difference across the membrane film can be calculated with Eq. (23):

$$dc = C_{mi} - C_{pi} = (C_i - C_{pi})\exp^{\frac{F_w}{k_d}} \tag{23}$$

Substituting Eq. (23) in to Eq. (7) yields:

$$C_{pi} = \frac{k_s\left(\frac{C_i + C_{i+1}}{2}\right)\exp^{\frac{F_w}{k_d}}}{F_w + k_s} \tag{24}$$

The concentration at the retained side (C_{i+1}) can be determined by Eq. (8), substituting the expression of C_{i+1} into Eq. (24), the solute permeate concentration with CP factor can be determined locally at each uniform slice by Eq. (25).

$$C_{pi} = \frac{k_{si} C_i \exp^{\frac{F_{wi}}{k_{di}}}}{F_{wi}\left(\frac{2-2r_i}{2-r_i}\right) + k_{si}\exp^{\frac{F_{wi}}{k_{di}}}} \tag{25}$$

In the determination of C_{pi} k_{si} and k_{wi} are assumed to be related to the membrane surface morphology and therefore varies locally. It should be noted that k_d can be related to the cross flow velocity and the geometry of the membrane channel by means of the following dimensionless analysis under laminar flow condition [28]:

$$\mathrm{Sh} = 1.86\mathrm{Re}^{0.33}\mathrm{Sc}^{0.33} = \frac{k_d d_h}{D} \tag{26}$$

$$\mathrm{Re} = \frac{v_i d_h \rho}{\mu} \tag{27}$$

$$\mathrm{Sc} = \frac{\mu}{D\rho} \tag{28}$$

where d_h is the hydraulic diameter of the membrane channel; ρ is the water density, and D is the salt diffusivity. Combing Eq. (26)–(28), the MTC k_d can be calculated with Eq. (29):

$$k_d = 1.86\left(\frac{D}{dh}\right)^{0.67}(v_i)^{0.33} \tag{29}$$

2.4. Nonhomogeneous diffusion

HSDM typically assumes a constant diffusivity across a nonporous, smooth, flat membrane surface where solute permeability is driven by the concentration gradient that exists between the feed and

permeate sides of the membrane. NHDM and NHDMCP incorporate surface roughness that effect mass transfer that can be quantified by considering the nonuniform structure of the membrane surface. Research conducted by Song and colleagues demonstrated that random distribution models can be used to describe heterogeneity of surfaces [29]. This mathematical approach was used to quantitatively describe the random distribution of the membrane's surface roughness. Continuous random heterogeneity would indicate that sites of ridge-and-valley morphology are randomly distributed over the entire surface of the membrane. The Gaussian distribution presented in Eq. (30) can be used to describe the thickness distribution of the membrane active layer.

$$P(z) = \frac{1}{\sigma_z\sqrt{2\pi}} \exp\left[-\frac{(z-\mu_z)^2}{2\sigma_z^2}\right] \tag{30}$$

where z is the localized membrane thickness, μ_z is the average of membrane thickness, and σ_z is the standard deviation of the membrane thickness.

The variations in membrane thickness were approximated numerically using a random Gaussian distribution generation function embedded in MATLAB (NORMRND) [19]. This function can be used to model the surface roughness variations of the membrane using the mean value of membrane thickness and an assumed standard deviation as function input parameters. NORMRND is anticipated to generate a set of random vectors that represent the active polyamide layer thickness and provide a picture of the active membrane layer shown as a three-dimensional surface plot with a ridge and valley morphology. When the membrane surface is modeled to include surface roughness, the solute and water MTCs can also be expressed to vary as a function of membrane thickness. The overall MTCs (k_w, k_s) or water and solute are determined by fitting the plant monitored data into Eqs. (1) and (2). They will be used as the MTCs for HSDM and the mean values for NHDM and NHDMCP. The localized k_{wi} and k_{si} are determined by the following mathematical expression:

$$k_{si}, k_{wi} = \frac{k_s, k_w}{z}\mu_z \tag{31}$$

In an attempt to initially determine the relative merit of the nonhomogeneous diffusion for membrane processes, the NORMRND function was utilized to generate images of hypothetical membrane surfaces. The generated images were compared with actual membrane images produced using AFM. The AFM images of two types of RO membranes manufactured by Hydranautics (Oceanside, CA), namely the ESPA2 and the CPA3 membranes, are shown in Fig. 3(a) and (b), respectively.

To numerically generate a mathematical representation of the membrane surface, the mean thickness of the active layer was assigned as the mean value of the vector z and the standard deviation was interpreted as the roughness of the membrane surface. A thickness matrix can be generated to graphically and

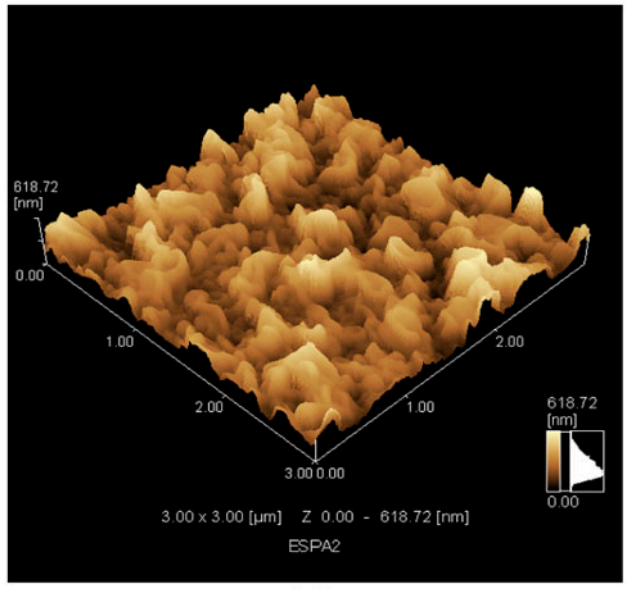

(a)

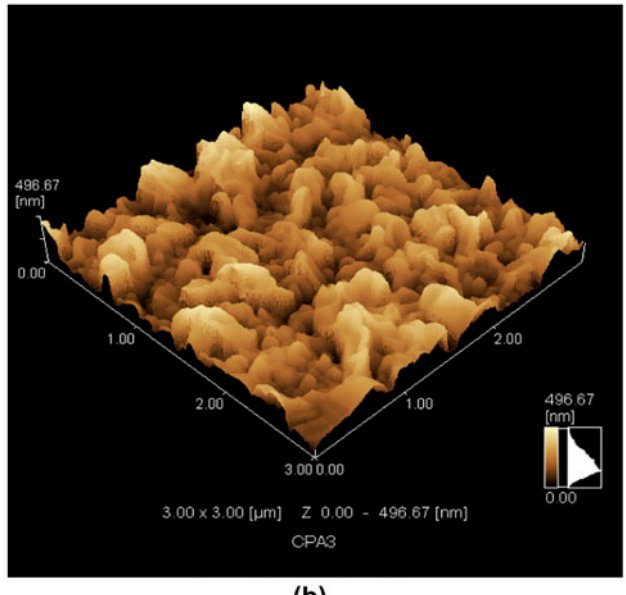

(b)

Fig. 3. AFM imagines of ESPA2 (a) and CPA3 (b) RO membranes (Courtesy of Hydranautics, Oceanside, CA).

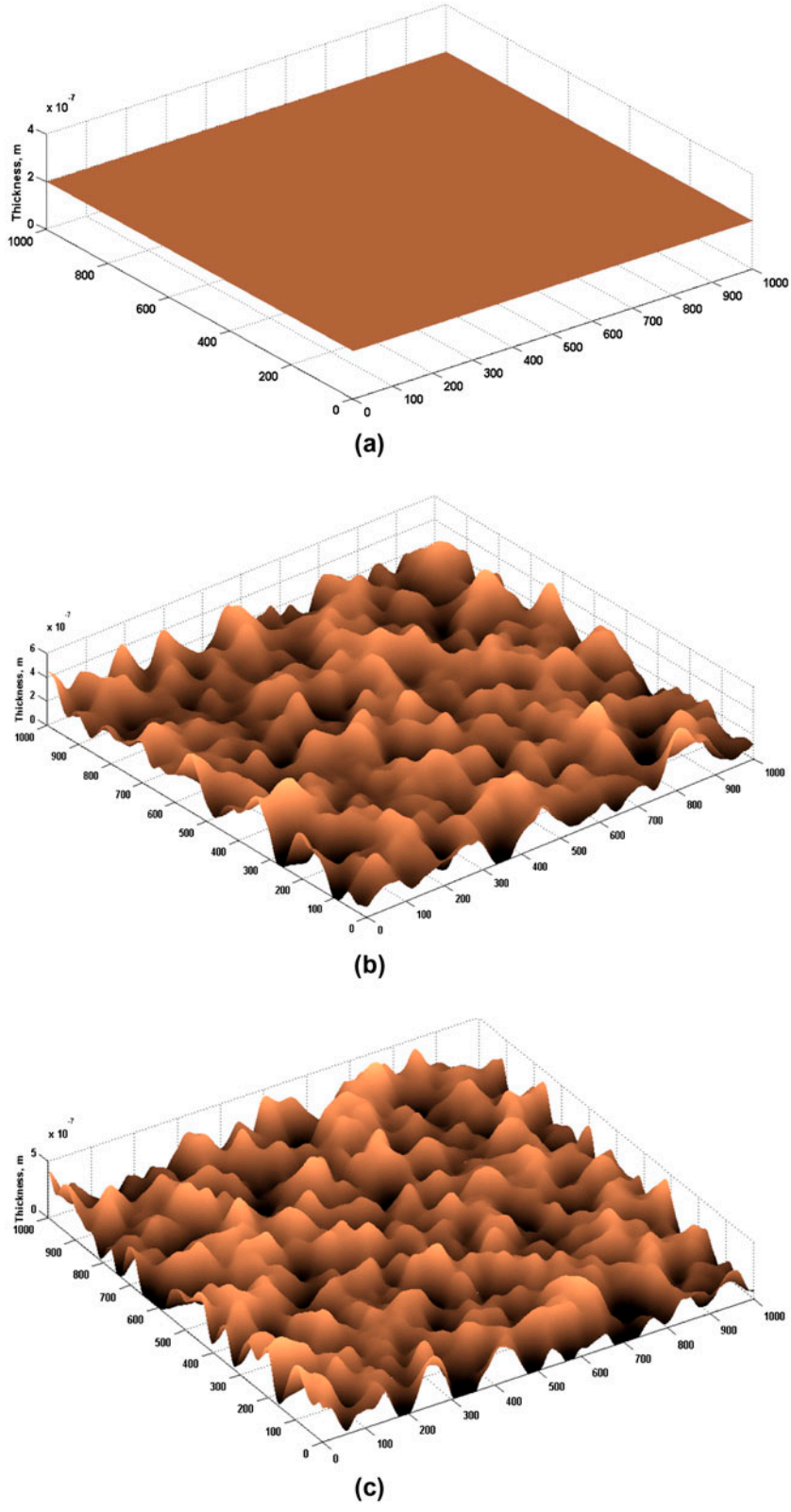

Fig. 4. Numercial plot of membranes surface stuctures of (a) flat; (b) ESPA2; (c) CPA3. Note that *X*- and *Y*- coordinates are the size of the random vector (z), with the Z-coodinate representing top layer thickness. Average thickness is 0.2 μm assumed for RO membrane manufactured by Hydranautics.

numerically represent the surface structure. To take into account different membrane properties, a smoothing script (SMOOTHN) was embedded into the thickness matrix calculations to reduce the influence of outlying data. Three different types of membranes are presented in Fig. 4 to demonstrate the combination of NORMRND and SMOOTHN functions. Fig. 4(a) represents the idealized, flat, homogeneous membrane surface, while Fig. 4(b) and (c) depict membranes with surface roughness similar to the AFM membrane images provided by Hydranautics (Oceanside, CA) in Fig. 3(a) and (b). Fig. 4(b) and (c) are visually comparable to Fig. 3(a) and (b), respectively. Based on this similarity, it was concluded that a mathematical approach of describing the variable membrane surface roughness was appropriate. Evaluating the applicability of nonhomogeneous diffusion was further validated through comparison of NHDM, NHDMCP, and HSDM predictions using pilot-scale data obtained from a brackish groundwater RO plant.

3. Results and discussion

3.1. Numerical simulation

Numerical simulation was implemented initially to develop the flow profiles in the membrane channel. This incremental representation of the flow rate through each uniform slice of the membrane channel allows for simulation of the solute concentration profile. These components are integrated into the NHDM/NHDMCP along with membrane surface considerations to predict permeate solute concentrations. Feed flow (Q_f), feed concentration (C_f), transmembrane pressure (Δp), and MTCs for water (k_w) and solute (k_s) are necessary to develop the flow rate and concentration profiles. These parameters were collected from ongoing pilot studies of a brackish groundwater desalination plant located in Sarasota, FL. Water qualities of the pilot plant were monitored for seven months in 2010. The pilot skid is a two-staged system with twelve four-inch diameter elements in the first stage and six four-inch diameter elements in the second stage. Each pressure vessel has three elements so there are six pressure vessels in operation for the pilot plant. During the course of the pilot study, water quality samples were collected and analyzed weekly. The operating conditions for the pilot plant skid in addition to the applicable water quality parameters are summarized in Table 1.

Sodium (Na^+) and potassium (K^+) were detected in the permeate stream at quantities above the minimum detection level and hence were chosen to serve as the water quality parameters that would be used for model fitting purposes. Numerous additional water quality parameters were analyzed including calcium, magnesium, sulfate, chlorides, alkalinity, hardness, and total dissolved solids; however, these were not used for model fitting. Table 1 indicates a range of feed water pH values for the pilot system. During the operational period of the pilot system, research was being conducted to assess the impacts of reducing and eliminating sulfuric acid pretreatment from the full-scale membrane process. This operational change is reflected in the feed water pH measurements collected during the pilot study, ranging from 5.8 to 7.1 pH units. However, this operational change in pH does not significantly affect the sodium or potassium concentrations, unlike the effects noted on hydrogen sulfide or bicarbonate alkalinity. The parameters used in the simulation are listed in Table 2.

To initiate the simulation, the membrane channel is divided into a finite number of uniform slices using a finite difference method to allow the water qualities to be determined locally. The average of sodium feed concentrations was used for both stages to demonstrate the simulations of HSDM, NHDM, and NHDMCP. The localized MTCs are shown in Figs. 5 and 6 for both stages. The flat horizon line represents the MTCs used in HSDM, where a homogeneous diffusion is assumed. The peak and bottom of k_{si} and k_{wi} an be related to the valleys and ridges on membrane surface. It is observed that faster mass transport occurs at the valleys of a membrane surface that contributes the majority of mass permeating the membrane, while the rest of the mass is retained at the ridges and passes through the membrane at a lower rate. The MTC (k_d) within the CP layer is depicted in Fig. 7 for each stage. k_d decreases in the cross flow direction due to a declined cross flow velocity along the membrane channel. It decreases at a slower speed in the second stage. This can be explained by an

Table 1
General information of RO pilot's data source

Parameter	Pilot system
Manufacturer	Hydranautics
Membrane element	CPA3–1st stage ESPA2– 2nd stage
Element area, sq ft	85
Feed flow, gpm	21.1
Recovery,%	75
Sodium concentration—feed, mg/L	284
Potassium concentration—feed, mg/L	6.2
Feed pH	6.9–7.3
Temperature, ˚C	23–30

Table 2
Parameters for simulation

Parameter	1st stage	2nd stage
Water density (25°C), kg/m^3	997×10^3	997×10^3
Water viscosity (25°C), N s/m^2	0.89×10^{-3}	0.89×10^{-3}
Diffusivity of sodium, m^2/s	1.33×10^{-9}	
Diffusivity of potassium, m^2/s	1.96×10^{-9}	
Feed channel height, m	7.9×10^{-4}	8.6×10^{-4}
Total length of channel, m	2.48	2.43
Channel width, m	0.917	0.917
Average velocity, m/s	0.13	0.11
Reynolds number (Re)	235	219
Water MTC (k_w), m/s-psi	8.05×10^{-8}	
Na MTC (k_s), m/s	1.57×10^{-7}	
K MTC (k_s), m/s	1.46×10^{-7}	
Number of uniform slice	1,000	1,000

enhanced CP effect in the second stage resulted from a higher solute concentration, which hinders the degree of k_d declining.

Once the MTCs are solved, the permeate flow (Q_{pi}) can be determined by Eq. (17) and simulated along the membrane channel with 1.33×10^{-3}m/s (21.1 gpm) as feed flow for the first stage and 6.12×10^{-4}m/s (9.7 gpm) for the second stage. The average sodium feed concentrations for the first stage and second stage are 300 mg/L and 615 mg/L, respectively, and were used as the initial concentration for simulation. Fig. 8 shows the permeate flow along the membrane channel. In the cross flow direction, the overall trend of permeate flow decreases as a result of the accumulated effect of pressure head loss and increased osmotic pressure. However, this effect is reduced by the thickness variation, where a higher permeate flow occurs at the valleys. In addition, the dependency of permeate flow on applied pressure was simulated for both stages and is shown in Fig. 9 (a) and (b). In both figures, when the applied pressure increases, the permeate flow increases but the increase rate declines toward the high end of the pressure range. When comparing the range of permeate flow for both stages, the permeate flow in the second stage increases in a lower rate than in the first stage within the same pressure increment. This observation indicates that with a higher salt feed concentration, increases in applied pressure are counted by increases in osmotic pressure, causing the permeate flux increases in a lower rate.

The solute concentration in the bulk flow C_i and on the membrane surface (C_{mi}) for each stage was determined by Eqs. (14) and (23) and are shown in Fig. 10(a) and (b). As the solute is incompletely rejected by the membrane, both C_i and C_{mi} increase along the membrane channel. The ridge and valley curve indicates the concentration on the membrane surface was affected by the surface morphology. The permeate concentration predicted by NHDM/NHDMCP at each stage are shown in Fig. 11(a) and (b). The permeate concentration increases in the cross flow direction. It is noted that the prediction by NHDMCP is affected by surface morphology, while the prediction by NHDM is less affected by surface morphology.

3.2. Prediction and comparison of NHDM/NHDMCP/HSDM

NHDM, NHDMCP, and HSDM were developed based on different membrane active layer topographies.

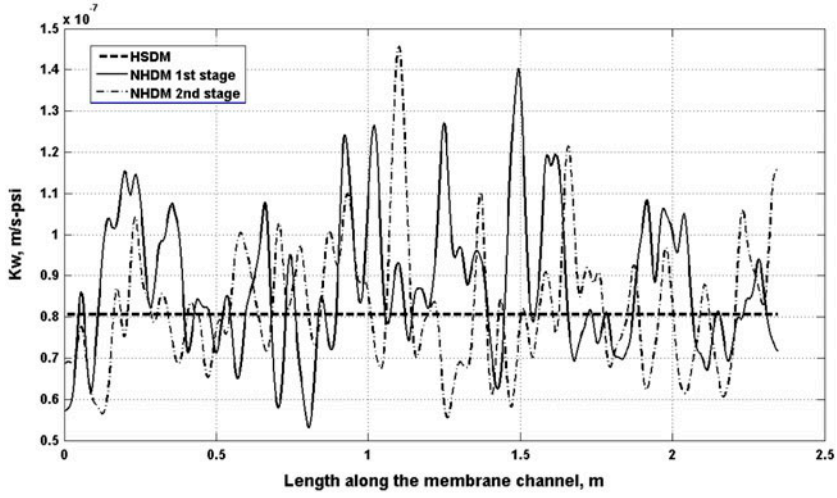

Fig. 5. Simulation of water MTCs for HSDM and NHDM/NHDMCP.

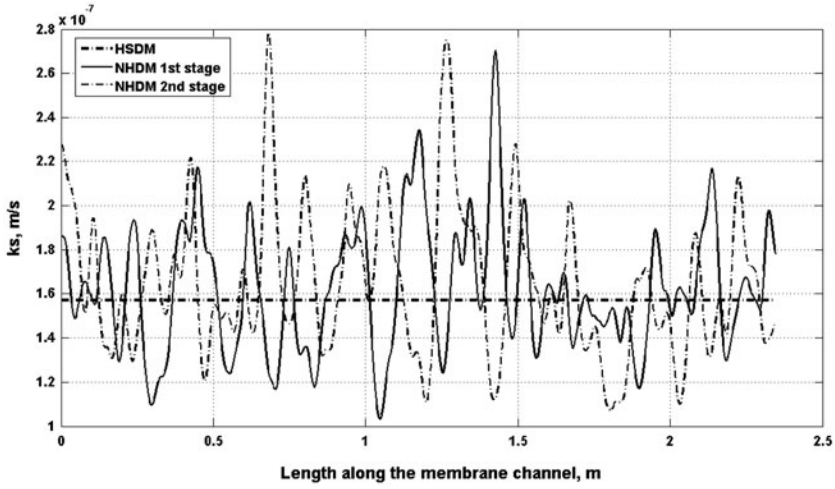

Fig. 6. Simulation of solute MTCs for HSDM and NHDM/NHDMCP.

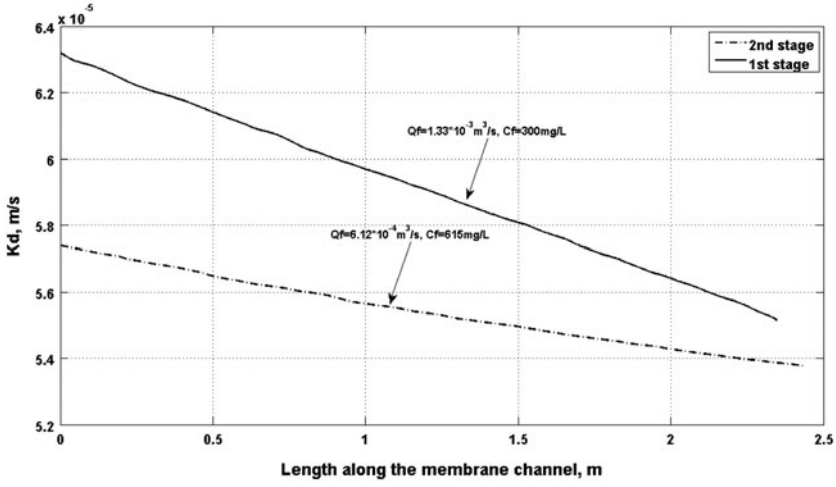

Fig. 7. Simulation of k_d along the membrane channel.

Fig. 4(a) demonstrates a HSDM application that assumes a flat surface and corresponding constant solute MTCs. As a comparison, a nonuniform active layer membrane surface depicted in Fig. 4(b) and (c) is incorporated into NHDM and NHDMCP. Model fitting and validation was conducted using data collected from pilot plant located at the city of Sarasota's 4.5 MGD brackish groundwater membrane desalination plant.

Assessment of NHDM, NHDMCP, and HSDM's performance was accomplished first by comparing model predictions with actual pilot-scale data. The predicted vs. actual plot for permeate concentration of sodium and potassium was developed in stages for each model. The models were then evaluated numerically through calculation of the average percent error (APE) between model predictions and full-scale data using Eq. (32). Qualitative assessment through observation of the predicted vs. actual plots along with comparison of calculated APE for each model were used to determine the relative performance of NHDM, NHDMCP, and HSDM as well as further assess the merit of the nonhomogeneous diffusion concept for salt passage in membrane processes.

$$\mathrm{APE} = \frac{|C_{\mathrm{actual}} - C_{\mathrm{predicted}}|}{C_{\mathrm{actual}}} \times 100\% \tag{32}$$

where C_{actual} is the actual permeate concentration and $C_{\mathrm{predicted}}$ is the predicted permeate concentration by NHDM/NHDMCP/HSDM.

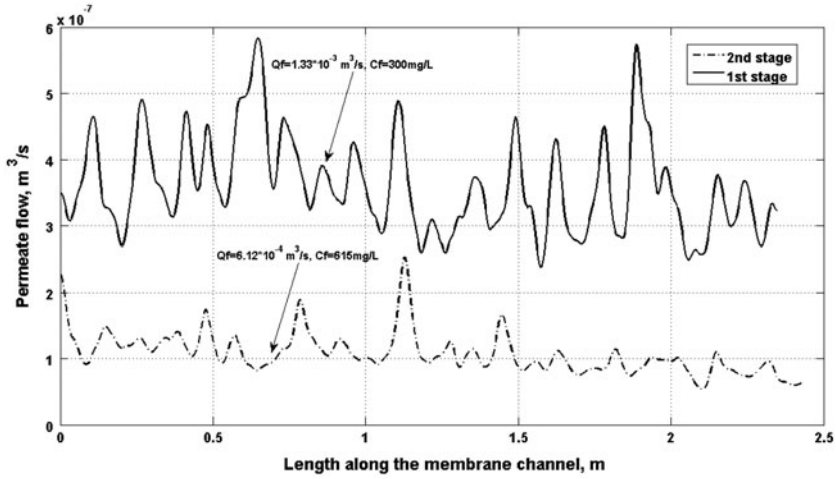

Fig. 8. Simulation of permeate flow along the membrane channel.

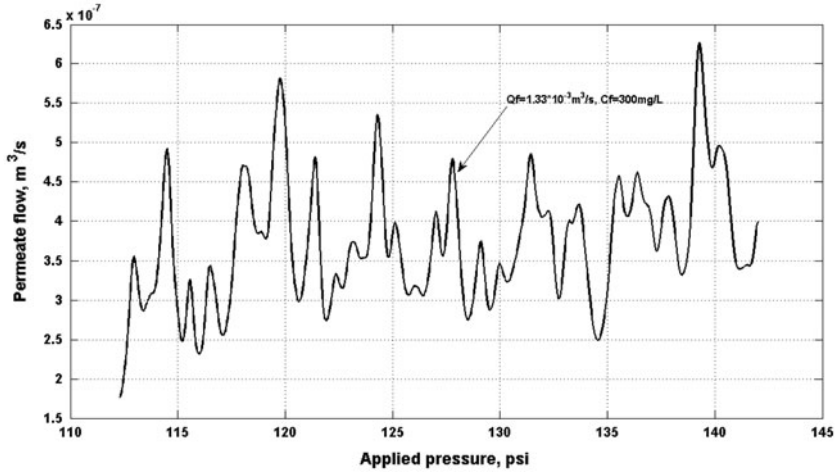

Fig. 9(a). Simulation of permeate flow versus applied pressure, 1st stage.

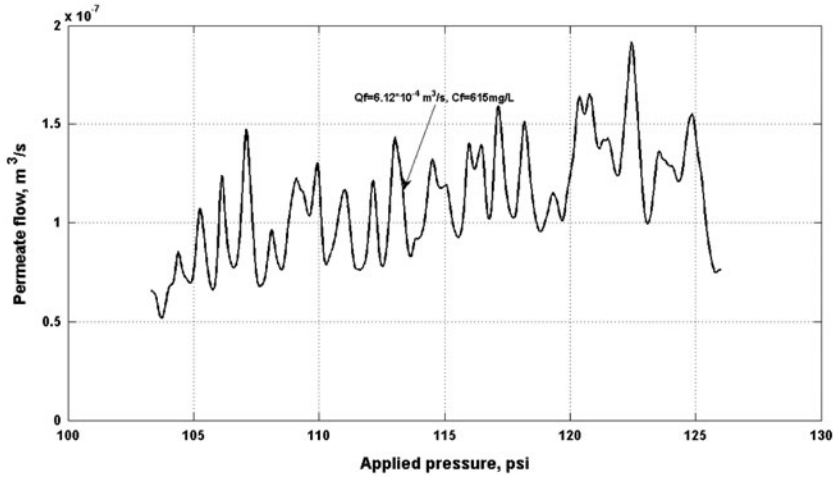

Fig. 9(b). Simulation of permeate flow versus applied pressure, 2nd stage.

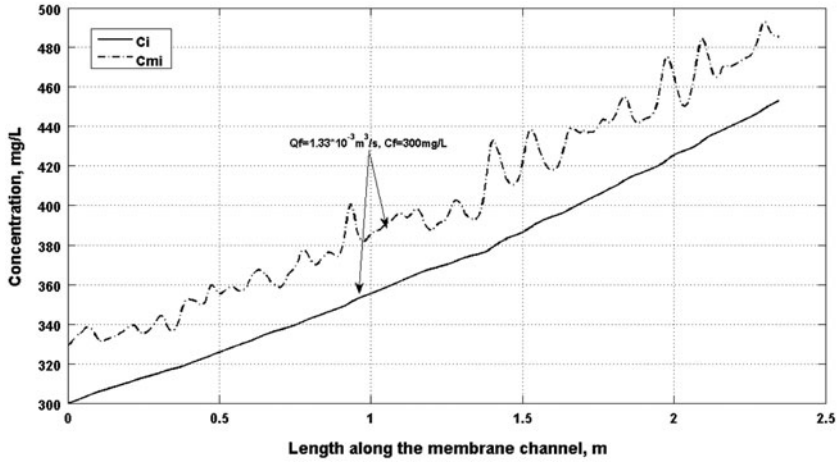

Fig. 10(a). Simulation of solute concentration in the bulk and on the membrane surface, 1st stage.

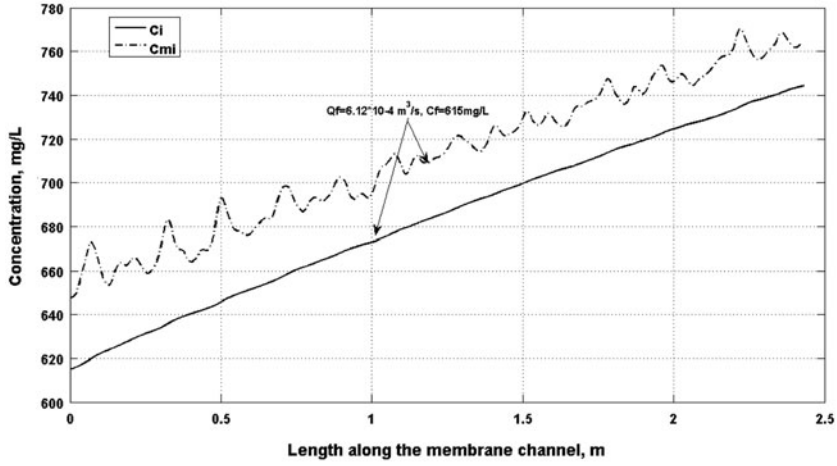

Fig. 10(b). Simulation of solute concentration in the bulk and on the membrane surface, 2nd stage.

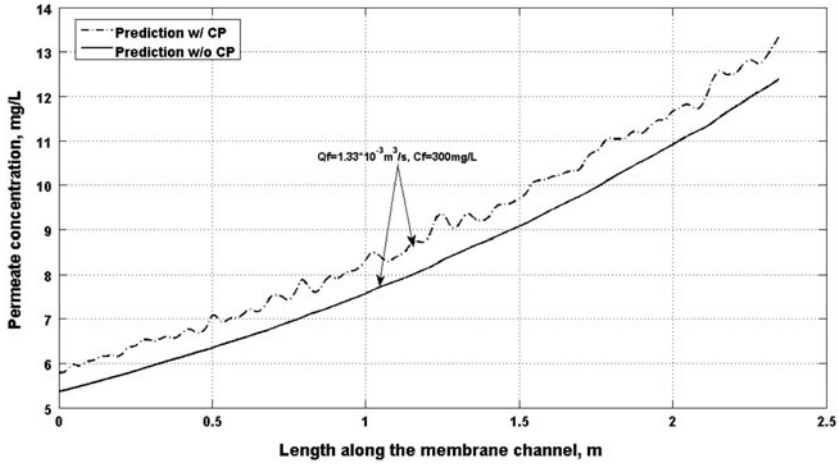

Fig. 11(a). Simulation of solute permeate concentration by NHDM/NHDMCP, 1st stage.

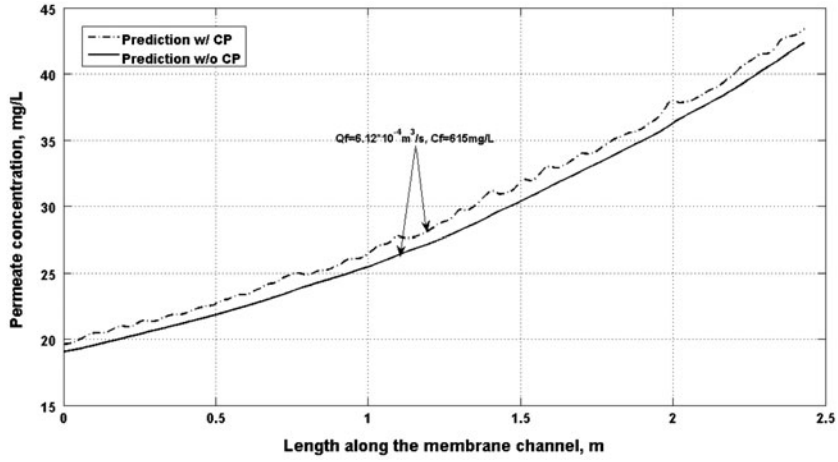

Fig. 11(b). Simulation of solute permeate concentration by NHDM/NHDMCP, 2nd stage.

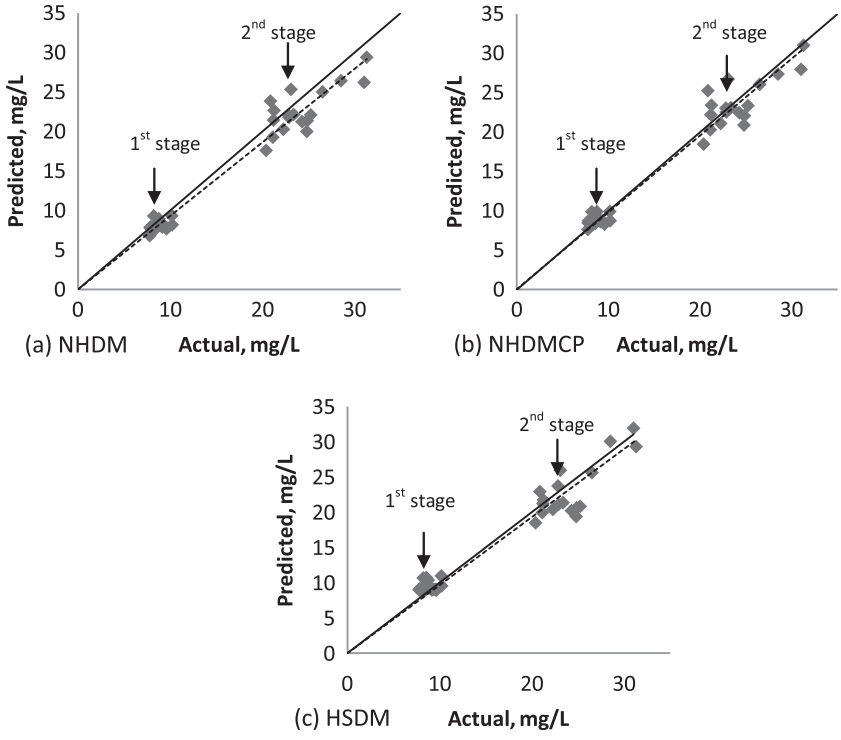

Fig. 12. Comparison of actual and simulated sodium concentration in permeate flow predicted by: (a) NHDM, (b) NHDMCP, and (c) HSDM.

Results of sodium predictions are presented in Fig. 12(a)–(c) by NHDM, NHDMCP, and HSDM. The solid lines represent the ideal line, where no error is observed between predicted and actual data, while the dashed lines represent the best numerical fit to the plot. The NHDM appears to under predict sodium permeate concentration for both stages, while the HSDM seems to over predict in the first stage and under predict the second stage. Prediction by NHDMCP is closer to the ideal prediction line, which shows improved accuracy compared with the other models. This suggests that the NHDMCP method shows improved accuracy with respect to predicting sodium permeate concentration for the conditions tested in the study. Predicted vs. actual plots for potassium are depicted in Fig. 13(a)–(c). The HSDM appears to over predict permeate concentrations in the first stage, while under prediction is observed for the

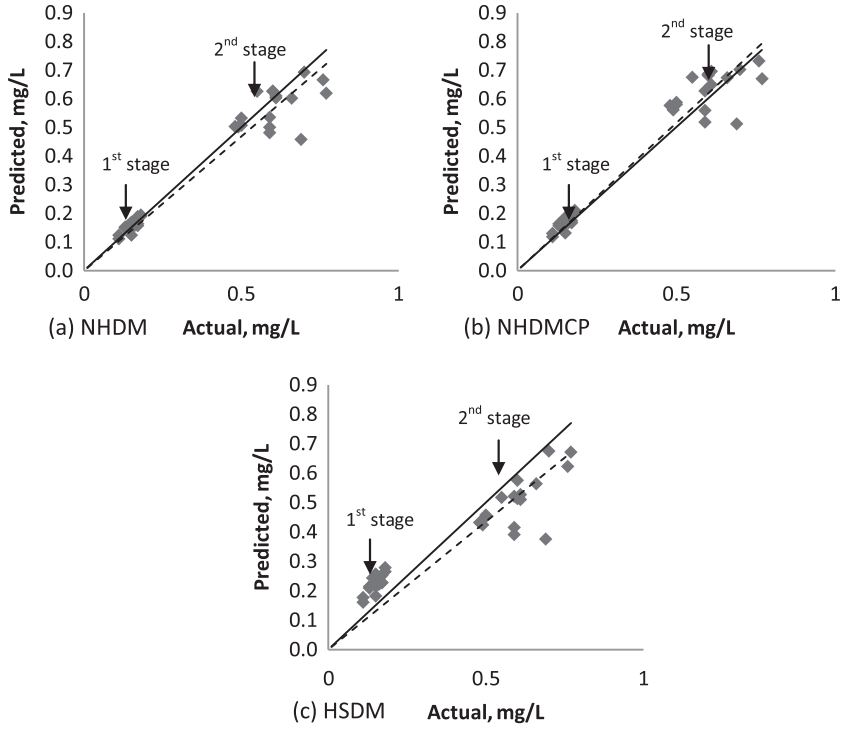

Fig. 13. Comparison of actual and simulated potassium concentration in permeate flow predicted by: (a) NHDM, (b) NHDMCP, and (c) HSDM.

second stage. Both NHDM and NHDMCP show more accurate prediction in both stages. Predictions by NHDMCP are closer to the ideal line. For potassium prediction, this qualitative analysis suggests that the NHCM and NHDMCP provide improved accuracy compared with HSDM.

Further accuracy comparisons were accomplished quantitatively through calculation of the APE between actual permeate solute concentrations and predicted concentrations. The results are shown in Figs. 14 and 15 for sodium and potassium, respectively. Fig. 14 illustrates that the weekly APEs for sodium appear to aggregate in a lower and narrower range for the NHDMCP, when compared with the HSDM and NHDM, while potassium appears to be predicted better by the NHDM. An overall APE determined for each model along with the associated standard deviations' results are summarized in Table 3. For sodium prediction, the overall APE and the standard deviation for the NHDMCP method are lower than the NHDM and HSDM methods. For potassium prediction, the NHDM appears to be a better model. This can be explained by the low concentration of potassium in the feed stream. With such a low concentration, the CP

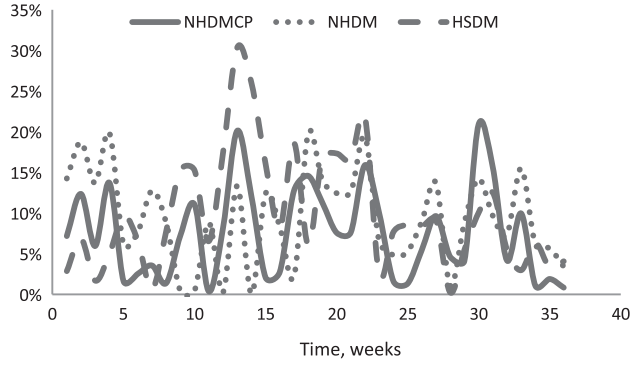

Fig. 14. Graphical presentation of weekly APE for sodium.

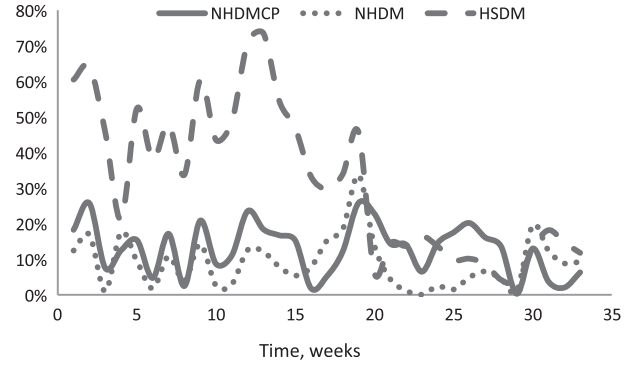

Fig. 15. Graphical presentation of weekly APE for potassium.

Table 3
Summarized APE for NHDMCP/NHDM/HSDM

	Sodium prediction		Potassium prediction	
	APE (%)	SD (%)	APE (%)	SD (%)
NHDMCP	7.6	5.5	13.0	7.0
NHDM	9.4	5.7	9.0	7.1
HSDM	10.0	7.0	32.2	20.6

might not be a significant factor, when predicting the permeate concentration. The data in Table 3 suggest that both NHDMCP and NHDM provide more accurate prediction of permeate sodium and potassium when compared with the HSDM. Consequently, consideration of nonhomogeneous diffusion in RO membrane processes may provide a more accurate prediction of solute permeate concentration, when using diffusion-based mass transfer models.

4. Conclusions

In this study, a nonhomogeneous diffusion model was developed with and without the CP effect and was compared with the homogeneous diffusion model. The mass transport across the membrane film was affected by the uneven morphology of the membrane surface. Mathematically, the uneven RO membrane active layer was created by a Gaussian random vector with a specified mean value and standard deviation. The NHDM and NHDMCP were developed based on this surface property and solved numerically to investigate the nonhomogeneous phenomenon assuming that solute and solvent MTCs vary with active layer thickness. By comparison, HSDM was studied based on a flat surface characteristic that assumes constant MTCs. Additional advantages of the nonhomogeneous approach include the ability to predict the hydraulic flow and solute concentration gradient in the bulk flow and on the membrane surface.

NHDM, NHDMCP, and HSDM were verified using pilot plant data from a brackish groundwater plant located in Florida. The relative performance of these three models was compared through development of predicted vs. actual plots and calculation of the APE for sodium and potassium. Observation of predicted vs. actual plots indicated that NHDMCP and NHDM predictions were in closer agreement with actual permeate concentrations. APE calculations indicated NHDMCP provides more accurate predictions of solute concentration with a high concentration in the feed stream, while NHDM appears to be a more accurate model, when predicting solute permeate concentration with a low feed concentration. This can be explained by the role of CP effect on mass transfer with different feed solute concentration. CP appears to be more significant in determining the salt passage, when the solute feed concentration is high. With further study on more solutes, a break point in feed stream concentration could be determined, where NHDMCP would be applied instead of NHDM.

Acknowledgments

The research was funded, in part, by UCF's Research Foundation through a grant provided by the Jones Edmunds Research Fund (Project 05-1620-0002 - RF1047820), as well as Funding Agreement 16208081 with the city of Sarasota, Florida. Any opinions, findings, and conclusions expressed in this material are those of the authors and do not necessarily reflect the views of UCF (Orlando, FL), its Research Foundation, Jones Edmunds Associates, Inc. (Gainesville, FL) or the city of Sarasota, Florida. The mention of trade names or commercial products does not constitute endorsement or recommendation. The authors acknowledge the help of Hydranautics (Oceanside, CA) in their providing UCF with AFM membrane images, without which this study would not have been made possible. The authors would like to thank Mr. Javier Vargas, Mr. Peter Perez and Ms. Katherine Gussie of the City of Sarasota's Public Works and Utilities Division (Sarasota, FL) for providing full-scale and pilot-scale reverse osmosis membrane process operations data that was relied upon for model development and validation. The contributions of UCF graduate students Mr. Jaya Tharamapalan and Mrs. Rebecca Wilder were significant; their efforts strengthened the results and their assistance was greatly appreciated.

Symbols and abbreviations

A	—	membrane active surface area, ft^2
α_1, α_2	—	constants in model equations
C_{fi}	—	feed concentration mg/L
C_{pi}	—	permeate concentration, mg/L
C_{ci}	—	concentrate concentration, mg/L
C_i, C_m	—	concentration in the membrane, mg/L
C_1	—	predicted TDS permeate concentration, ppm
C_2	—	actual TDS permeate concentration, ppm
Δc	—	concentration difference across the membrane film, mg/L

ΔC	—	concentration difference across the membrane unit in the bulk flow, mg/L
d	—	day
F_{wi}	—	solvent permeate flux, gal/sfd
J_i	—	solute permeate flux, mg/sfd
k_w	—	solvent mass transfer coefficient, gal/sfd-psi
k_{si}	—	solute mass transfer coefficient, gal/sfd
k_t	—	solvent mass transfer coefficient, gal/sfd-psi
n	—	amount of element unit
Δp	—	applied pressure difference, psi
$\Delta\pi$	—	osmotic pressure difference, psi
Q_{fi}	—	feed flow, gpm
Q_{pi}	—	permeate flow, gpm
Q_{ci}	—	concentrate flow, gpm
Q_i, Q_m	—	volumetric flow in the membrane, m^3/s
ΔQ	—	flow difference across the membrane unit in the bulk flow, m^3/s
R	—	overall recovery, %
r	—	unit element recovery, %
μ_z	—	mean of random vector
σ_z	—	standard deviation of random vector
z	—	active layer thickness, m
HSDM	—	homogeneous solution diffusion model
NHDM	—	nonhomogeneous solution diffusion model
NHDMCP	—	nonhomogeneous solution diffusion model with concentration polarization

References

[1] Y. Zhao, J.S. Taylor, Incorporation of osmotic pressure in an integrated incremental model for predicting RO or NF permeate concentration, Desalination 174 (2005) 145–159.

[2] Y. Zhao, J.S. Taylor, Assessment of ASTM D 4516 for evaluation of reverse osmosis membrane performance, Desalination 180 (2005) 231–244.

[3] K. Jamal, M.A. Khan, M. Kamil, Mathematical modeling of reverse osmosis system, Desalination 160 (2004) 29–42.

[4] Y. Zhao, J.S. Taylor, S. Chellam, Predicting RO/NF water quality by modified solution diffusion model and artificial neural networks, J. Membr. Sci. 263 (2005) 38–46.

[5] S.J. Duranceau, Modeling the permeate transient response to pertubation from steady state in a nanofiltration process, Desal. Water Treat. 1 (2009) 7–16.

[6] M.P.S. Ramani, Mass transport mechenism of the high-pressure side in reverse osmosis: an analysis, Chem. Eng. Sci. 47 (1991) 4099–4105.

[7] B. Absar, O. Belhamiti, Reverse osmosis modeling with orthogonal collocation of finite element method, Desal. Water Treat. 21 (2010) 23–32.

[8] D. Cheddie, A. Maharajh, A. Ramkhalawan, P. Persad, Transient modeling of wave powered reverse osmosis, Desalination 260 (2010) 153–160.

[9] K. Spiegler, O. Kedem, Thermodynamics of hyperfiltration (reverse osmosis): Criteria for efficient membrane, Desalination 1 (1966) 311–326.

[10] N. Park, S. Lee, S.-H. Lee, Mass transfer of bacterial by-product (BBP) during nanofiltration: Characterizations, transport, and sherwood relationships, Desalination 247 (2009) 623–635.

[11] V. Gekas, B. Hallstrom, Mass transfer in the membrane concentration polarization layer under turbulent cross flow-critical literature review and adaptation of existing sherwood correlations to membrane operations, J. Membr. Sci. 30 (1987) 153–170.

[12] V. Gekas, K. Olund, Mass transfer in the membrane concentration polarization layer under turbulent cross flow-applucation of the chaacterization of ultrafiltration membranes, J. Membr. Sci. 37 (1988) 145–163.

[13] F. Li, W. Meindersma, A.B. Haan, T. Reith, Optimization of commercial net spacers in spiral wound membrane modules, J. Membr. Sci. 208 (2002) 289–302.

[14] S.A. Avlonitis, D.G. Pavlou, S. Skourtis, Simulation of the spiral wound RO membranes deformation under operating conditions, Desal. Water Treat. 25 (2011) 91–97.

[15] N.Y. Yip, A. Tiraferri, W.A. Phillip, J.D. Schiffman, M. Elimelech, High performance thin-film composite forward osmosis membrane, Environ. Sci. Technol. 44 (2010) 3812–3818.

[16] S.M.S. Ghiu, R.P. Carnahan, M. Barger, Permeability of electrolytes through a flat RO membrane in a direct osmosis study, Desalination 144 (2002) 387–392.

[17] E.M. Vrijenhoek, S. Hong, M. Elimelech, Influence of membrane surface properties on initial rate of colloidal fouling of reverse osmosis and nanofiltration membranes, J. Membr. Sci. 188 (2001) 115–128.

[18] M. Elimelech, X. Zhu, A. Childress, S. Hong, Role of membrane surface morphology in colloidal fouling of cellulose acetate and composite aromatic polyamide reverse osmosis membranes, J. Membr. Sci. 127 (1997) 101–109.

[19] MATLAB version 7.10.0. The MathWorks, Natick, MA, 2010.

[20] N.A. Gjostein, Non-Homogeneous Diffusion. Diffusion (Chapter 9). American Society for Metals, Metals Park, OH, 1972.

[21] Y. Zhao (2004). Modeling of Membrane Solute Mass Transfer in NF/RO System Membrane Systems. PhD dissertation, University of Central Florida.

[22] S.S. Chen, Modeling of Membrane Surface Chemistry and Mass Transfor., PhD dissertation, University of Central Florida, 1999.

[23] L-K. Sung, Film-Theory and Ion Coupling Models for Diffusion Controlled Membrane Processes, PhD dissertation, University of Central Florida, 1993.

[24] J.S. Taylor,E.P. Jacobs, Reverse osmosis and nano-filtration,in J. Malleviablle, P.E. Odendaal ,M.R. Wiesner, Water treatment membrane process (Chapter 9), McGraw-Hill,1996.

[25] Standard practice for standardizing reverse osmosis performance data. (2010). Annual Book of ADTM Standards. D4516–65.

[26] C.R. Bouchard, P.J. Carreau, T. Matsuura, S. Sourirajan, Modeling of ultrafiltration: Prediction of concentration polarization effect, J. Membr. Sci. 97 (1994) 215–229.

[27] M.R. Wiesner, R. Aptel, Mass transport and permeate flux and fouling in pressure-driven process, in J. Mal-levialle, P.E. Odendaal, M.R. Wiesner, Water Treatment Membrane Processes (Chapter 4), McGraw-Hill, 1996.

[28] M. Isaacson, A. Sonin. Sherwood number and friction factor correlations for electrodialysis system, with application to process optimization. Ind. Eng. Chem. Process Des. Dev. 15 (2) (1976) 313–321.

[29] L. Song, P. Johnson, M. Elimelech, Kinetics of colloid deposition onto heterogeneously charged surfaces in porous media, Enviorn. Sci. Technol. 28 (1994) 1164–1171.